Ancient papyrus scroll-inspired self-deployable mechanism based on shape memory polymer composites for Mars explorations

Dou Zhang [a], Liwu Liu [a], Pengfei Xu [a], Yinzhong Zhao [b], Qifeng Li [c], Xin Lan [c], Xin Zou [d], Ying Li [d], Yanchun He [b], Yanju Liu [a,*], Jinsong Leng [c,*]

[a] Department of Astronautical Science and Mechanics, Harbin Institute of Technology, Harbin 150001, People's Republic of China
[b] Science and Technology on Vacuum Technology and Physics Laboratory, Lanzhou Institute of Technology, Lanzhou 730000, People's Republic of China
[c] Centre for Composite Materials and Structures, Harbin Institute of Technology, Harbin 150080, People's Republic of China
[d] Beijing Institute of Spacecraft System Engineering, Beijing 100094, People's Republic of China

ARTICLE INFO

ABSTRACT

Mars has similar natural environments to Earth and is regarded as a potential candidate for human migration. Exploration to Mars has been a hotspot in major aerospace countries, and therefore bringing the national flag to Mars is an inevitable demand. A self-deployable mechanism inspired by the ancient papyrus scroll to demonstrate the national flag dynamically is proposed in this paper. The release device made of shape memory polymer composites, as the functional part, is analysed thoroughly from the perspective of material design, fabrication and experiments. Firstly, the mechanical properties of woven fabric composites are predicted theoretically, and the thickness of laminates is determined according to the mechanical requirement, fabrication technique and shape moulding method. Tensile and three-point bending tests were carried out to validate the analytical prediction and provide parameters for numerical simulation. Besides, shape fixation and recovery properties were studied by both simulation and experiments with consistent results. Additionally, the shape moulding method was modified by reheating and sustaining a high-temperature period after bending to obtain the designed pattern. This world's first application of shape memory polymer composites in Mars explorations is a milestone for both deep space exploration and advanced smart materials.

1. Introduction

Deep space exploration involves exploring distant regions of outer space. The United States and the Soviet Union began to launch deep space probes to explore the solar system in 1957. During the last fifty years, deep space missions have covered all kinds of solar system celestial bodies. Several countries such as the United States, the Soviet/Russia, Japan, the European Union, and China have successfully carried out independent deep space exploration missions [1]. These activities enable humans to understand the Earth, the solar system and the universe. The giant stride facing humans is shifting from landing on the Moon to migrating to Mars because Mars is the hope of humanity. Three billion years ago, Mars was believed to have a warm and humid climate, a strong magnetic field, a dense atmosphere and other natural environments similar to Earth's. These conditions are crucial to the survival of life. Therefore, whether there was such a period on Mars is the key to answering whether there is only life on Earth. Besides, whether Mars is

suitable for large-scale migration still has many scientific and technical problems to be solved. In 2020, humankind ushered in three Mars exploration missions [2]. On 20th July, with the technical support of the United States, the United Arab Emirates' "Hope" Mars orbiter, the first interstellar exploration in the Arab World, was launched in Japan [3]. On 23rd July, China successfully launched the "Tianwen-1″ Mars probe with the "Long March-5″ rocket [4]. It was China's first independently developed Mars exploration mission, including an orbiter, lander and rover. It performed circumnavigation, landing and inspection in one task. On 30th July, NASA's Mars probe "Perseverance" was launched from Cape Canaveral Air Force Base in Florida [5,6]. Based on the "Curiosity" mission [7], it collected and stored geological samples that may contain evidence of alien life, planning to bring them back to Earth in the next mission.

Mars exploration is challenging because the distance between Mars and Earth ranges from 54 million to 400 million kilometres. Probes need to get rid of the Earth's gravity first and then be captured by the gravity of Mars, placing high demands on the rocket. Therefore, advanced

---

Nomenclature

a_w	width of warp yarn cross-section
a_f	width of fill yarn cross-section
$a_{ij}(x,y), b_{ij}(x,y), d_{ij}(x,y)$	in-plane compliance matrices for a quarter of unit cell
$\vec{a}_{ij}^{\,s}(y), \vec{b}_{ij}^{\,s}(y), \vec{d}_{ij}^{\,s}(y)$	in-plane compliance matrices along X-axis
$\vec{a}_{ij}^{\,sp}$	in-plane tension stiffness matrix for the whole unit cell
$A_{ij}(x,y), B_{ij}(x,y), D_{ij}(x,y)$	in-plain stiffness matrices for a quarter of unit cell
$\vec{A}_{ij}^{\,s}(y), \vec{B}_{ij}^{\,s}(y), \vec{D}_{ij}^{\,s}(y)$	in-plane stiffness matrices along X-axis
$\vec{A}_{ij}^{\,sp}, \vec{B}_{ij}^{\,sp}, \vec{D}_{ij}^{\,sp}$	in-plane stiffness matrices for the whole unit cell
b	specimens' width in three-point bending tests
d	specimens' thickness in three-point bending tests
D	maximum deflection of specimens in three-point bending tests
$e_f(y)$	boundary of fill yarn that does not intersect with the warp yarn
$e_w(x)$	boundary of warp yarn that does not intersect with the fill yarn
ε_f	flexural strain from three-point bending tests
E_f	flexural modulus from three-point bending tests
E_1^f	longitudinal Young's modulus of the fibre
E_2^f	transverse Young's modulus of the fibre
E^m	tensile modulus of the matrix
E_1^s	longitudinal Young's modulus of the fibre strand
E_2^s	transverse Young's modulus of the fibre strand
E_x, E_y, E_z	tensile moduli of WF composites
$E_x^{45°}$	in-plane tensile modulus of WF composites oriented at $\pm 45°$
F	load in three-point bending tests
g_f	gap between adjacent fill yarns
g_w	gap between adjacent warp yarns
G_{12}^f	in-plane shear modulus of the fibre
G^m	shear modulus of the matrix
G_{12}^s	in-plane shear modulus of the fibre strand
G_{23}^s	out-of-plane shear modulus of the fibre strand
G_{yz}, G_{zx}, G_{xy}	shear moduli of WF composites
h	ply thickness of WF composites
h_f	thickness of fill yarn cross-section

h_w	thickness of warp yarn cross-section
h_t	thickness of WF fabric
$H_f(x)$	centre of the fill yarn
$H_w(y)$	centre of the warp yarn
l_y	width of the unit cell
L	specimens' support span in three-point bending tests
ρ	radius of curvature
ρ_0	initial radius of curvature
ρ_t	radius of curvature at time t
Q_{ij}^e	stiffness matrix
$\overline{Q}_{ij}^e$	transformed stiffness matrix
R	Reuter matrix
R_t	recovery ratio
T_{ij}^f	global–local stress transformation matrix of the fill yarn
T_{ij}^w	global–local stress transformation matrix of the warp yarn
u_f	undulation of fill yarns
u_w	undulation of warp yarns
ν_{12}^f	in-plane Poisson's ratio of the fibre
ν_{23}^f	out-of-plane Poisson's ratio of the fibre
ν_{12}^s	axial in-plane Poisson's ratio of the fibre strand
ν_{21}^s	transverse in-plane Poisson's ratio of the fibre strand
ν_{23}^s	out-of-plane Poisson's ratio of the fibre strand
ν^m	Poisson's ratio of the matrix
$\nu_{xy}, \nu_{xz}, \nu_{yz}$	Poisson's ratios of WF composites
V_f^s	fibre volume fraction in a fibre strand
$\theta_f(x)$	local angels between the fill yarn and global X-axis
$\theta_w(y)$	local angels between the warp yarn and global Y-axis
σ_f	flexural stress obtained from three-point bending tests
CFRP	carbon fibre reinforced plastic
CLT	classical lamination theory
CNC	computer-numerical-controlled
DMA	dynamic mechanical analysis
PS	parallel-series
SMP	shape memory polymer
SMPC	shape memory polymer composite
SP	series–parallel
Tg	glass transition temperature
UD	unidirectional
WF	woven fabric

composites with superior and distinctive properties have attracted much attention [8,9]. Carbon fibre fabric with low density, high modulus, and good thermal and electrical conductivities is the most widely used reinforcement [10–12]. Liu et al proposed a deployable cabin based on carbon fibre reinforced plastics (CFRPs) [13,14]. The analytical investigation, numerical simulation and physical experiments were conducted to predict the effect of geometric parameters on the cabin's folding behaviour. This structure is regarded as a promising habitat in deep space exploration. In addition to the load-bearing function, smart materials can also serve as functional components [15,16]. Among them, shape memory polymers (SMPs) are typical smart materials that can maintain a temporary configuration and recover their original shape under external stimuli such as heat, light, electric field and magnetic field etc. [17]. Nonetheless, the relatively low strength and stiffness have restricted their applications in aerospace, which can be figured out by adding reinforcements. Therefore, carbon fibre reinforced shape memory polymer composites (SMPCs) have spread their applications to various structures, such as hinges, booms, solar arrays and antennas [18–23]. Woven fabric (WF) composites are a class of textile composites

with two or more yarns interlaced at an angle [24]. They provide more balanced in-plane properties, higher inter-laminar shear strength and better impact tolerance than unidirectional (UD) composites [25]. The interlacing of yarns leads to higher out-of-plane strength. Besides, the fabrication of WF composites is less laborious due to the easier handling of woven fabrics, resulting in reduced fabrication errors and lower manufacturing costs. However, these advantages are achieved at the expense of in-plane stiffness and strength due to the tow waviness. Modelling techniques for predicting the mechanical properties of WF composites are therefore necessary to design laminate for applications. The finite element analysis of repeating unit cells predicts the properties [26], and analytical models rely on the underlying assumption that classical lamination theory (CLT) applies to each slice of the unit cell [27].

In this work, an ancient papyrus scroll-inspired mechanism released by SMPCs is proposed. Compared with pasting the flag on a fixed surface, it has a dynamic deployment. This paper is documented in the sequence of structure presentation, material design and verification, shape memory simulation and experiments. Firstly, the structure of the
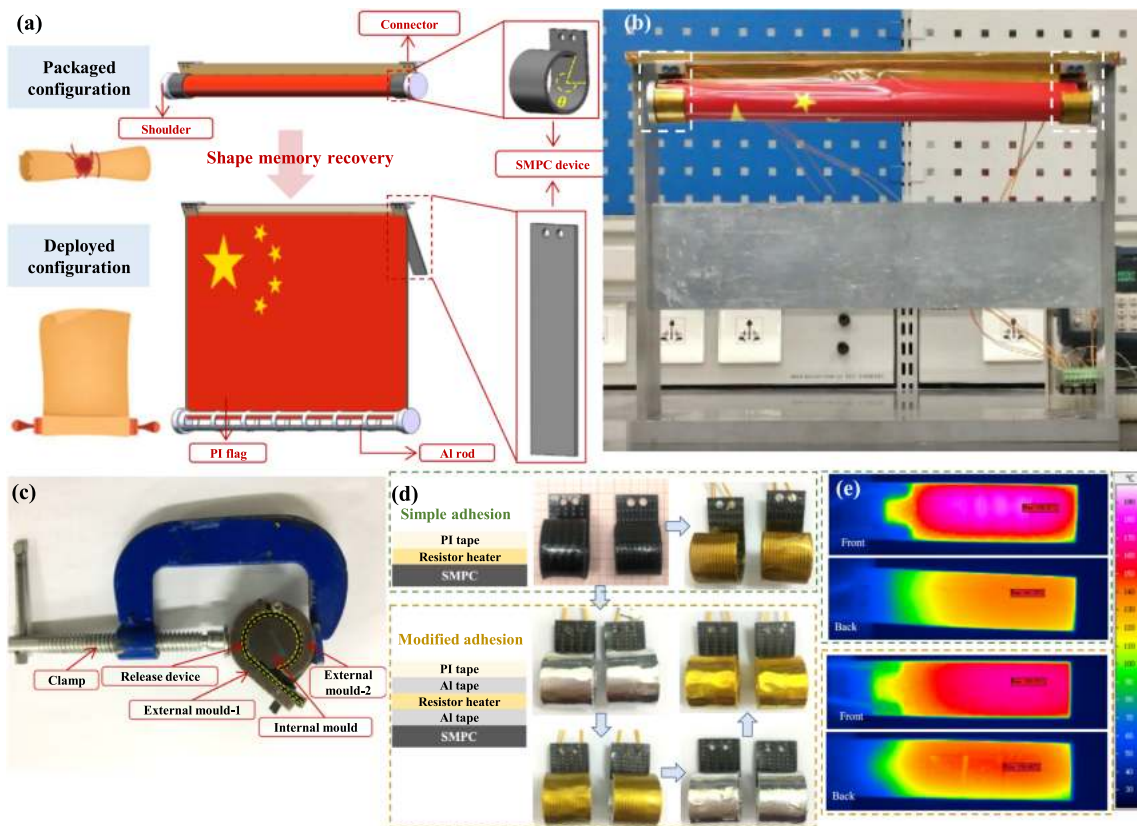
Fig. 1. Papyrus scroll-inspired mechanism, (a) schematic of self-deployable mechanism with packaged and deployed configurations, (b) assembled mechanism with SMPC devices framed in white dashed lines, (c) apparatus for shape moulding of SMPC devices, (d) two adhesion methods for resistor heaters and (e) infrared thermal images of devices with two different adhesion methods under the same power supply (28 V).

ancient papyrus scroll mechanism is introduced, with its working principle elaborated. Then, the mechanical properties of SMPCs reinforced by woven carbon fabric with yarn undulation are predicted. Together with the fabrication technique, shape moulding and weight reduction considerations, the thickness of the laminate is determined. Besides, specimens fabricated by the resin infusion method are tested in tension and three-point bending. Shape fixation and recovery properties are evaluated by finite element analysis and experiments. Additionally, the shape moulding method is further modified to improve the bent configuration of SMPCs. The ground-based validation and on-Mars qualification have been presented in our previous work [28], and this paper focuses on the material design and deployment verification.

2. Design and analysis of the papyrus scroll-inspired mechanism

2.1. Concept of the papyrus scroll-inspired mechanism

An ancient papyrus scroll-inspired architecture in Fig. 1 (a) has been proposed in [28]. It is a self-deployable mechanism released by SMPCs to exhibit important information such as the national flag or mission code after landing. It consists of five components: two SMPC devices, a national flag printed on a PI membrane, a hollowed Al rod, two shoulders and two connectors. Firstly, the packaged configuration is achieved by SMPC devices in the curved configuration. The flag and SMPC devices are fixed to the connectors through-bolt connection. The Al rod is glued to the bottom of the flag and acted as a roller when packaging the mechanism. When the flag is rolled up, two shoulders are assembled to both ends of the Al rod through threads to restrict the axial displacement. The circumferential displacement is limited by two bent SMPC devices. Hence, the packaged mechanism is obtained and can be installed on the landing platform through connectors. Then, the
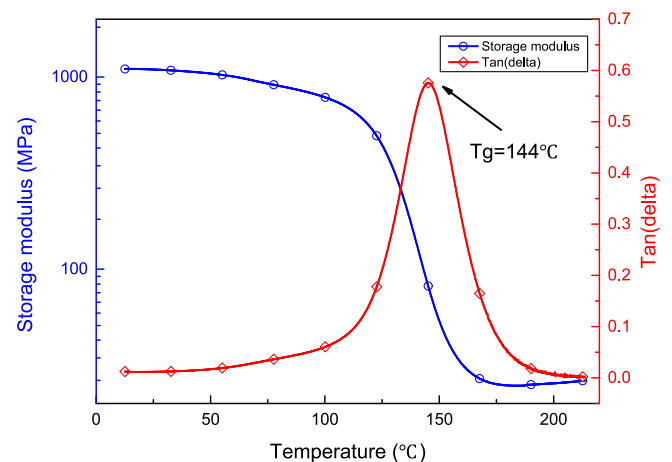
Fig. 2. Thermo-dynamic mechanical properties of SMP matrix.

deployment is triggered by the shape memory recovery of SMPC devices. The curved SMPCs recover their original flat shape when perceiving external stimuli, and the flag is flattened when the Al rod falls under Martian gravity. Compared with sticking the flag directly on the lander's surface, which was used in the "Chang'e-3″ mission [29], the proposed structure presents a dynamic and vivid demonstration. Besides, the flag can flutter in the Martian wind [30].

2.2. Material design and structural assembly

According to the analysis of five components, the only one that needs

Table 1
Elastic properties of the fibre and matrix.

Material	E_1(GPa)	$E_2 = E_3$(GPa)	$G_{12} = G_{13}$(GPa)	G_{23}(GPa)	ν
Carbon fibre [39]	230.0	40.0	24.0	14.3	0.26
Epoxy resin	0.98	0.98	0.36	0.36	0.35[34]

to be further studied is the SMPC device. It is the functional part that packages and deploys the flag. Therefore, the laminate design will be carried out in this section. Firstly, the matrix used is epoxy-based SMP developed by Jinsong Leng's group [31], which has already been successfully used in aerospace [32,33]. The glass transition temperature (*Tg*) for the SMP matrix was tested on a DMA (dynamic mechanical analysis) analyzer (NETZSCH Instruments, Germany) with a tension oscillatory temperature from 25 ℃ to 220 ℃. The heating rate and frequency were set to be 3 ℃/min and 2 Hz, respectively. Specimens for those tests were processed into a dimension of 60 mm × 5 mm. The storage modulus and tan(delta) as a function of temperature are illustrated in Fig. 2. SMPs go through three stages as the temperature increases: glassy state, glass transition stage, and rubbery state. The storage modulus decreases by more than two orders of magnitude, from 1184 MPa to about 10 MPa. As the ratio of the loss modulus to the storage modulus, the loss factor tan(delta) represents an "Ω" shape. *Tg* is defined by the temperature corresponding to the peak value of tan (delta), and it is approximately 144 ℃.

In addition, the tensile modulus of the matrix E^m in Table 1 is measured by simple tension tests and Poisson's ratio ν^m is inherited from the literature [34]. The shear modulus G^m is not measured but calculated by the following equation for the isotropic material:

$$G^m = \frac{E^m}{2(1 + \nu^m)} \tag{1}$$

Mechanical properties of WF composites are governed by the fabric geometry, strength, yarn undulation (waviness) and constituents' properties. The orientation and density of fabrics are two design parameters. Firstly, the orientation is selected to be ± 45° to accommodate the bending deformation, empirically [18]. Considering that the yarn undulation drastically degrades the enhancing effect of WF composites compared to the UD lamina, we use the CLT to obtain effective mechanical constants [35–38]. After comprehensively considering the mechanical requirement and fabrication technique, the SMPC's thickness is determined.

The warp and fill yarns in Fig. 3 were modelled as angle-ply laminates to predict the in-plane elastic constants. The mechanical properties of carbon fibre in Table 1 are obtained from the literature [39].

Firstly, the mechanical parameters of the fibre yarn in Table 2 are predicted as follows. The longitudinal Young's modulus of the fibre strand E_1^s is predicted by the rule of mixture:

$$E_1^s = V_f^s E_1^f + (1 - V_f^s)E^m \tag{2}$$

where V_f^s is 0.64, representing the fibre volume fraction in a fibre strand and is obtained from the literature [39]. The transverse Young's modulus of the fibre strand E_2^s is calculated using the semi-empirical Halpin-Tsai formulation with the parameter $\xi = 1$ as suggested by Daniel and Ishai [40]:

$$E_2^s = \frac{E^m(1 + \xi\eta_2 V_f^s)}{(1 - \eta_2 V_f^s)} \tag{3}$$

Table 2
Mechanical properties of the carbon fibre/epoxy strand.

E_1^s(GPa)	$E_2^s = E_3^s$(GPa)	$G_{12}^s = G_{13}^s$(GPa)	G_{23}^s(GPa)	$\nu_{21}^s = \nu_{31}^s$	ν_{23}^s	V_f^s
147.78	4.05	1.95	1.57	0.008	0.29	0.64
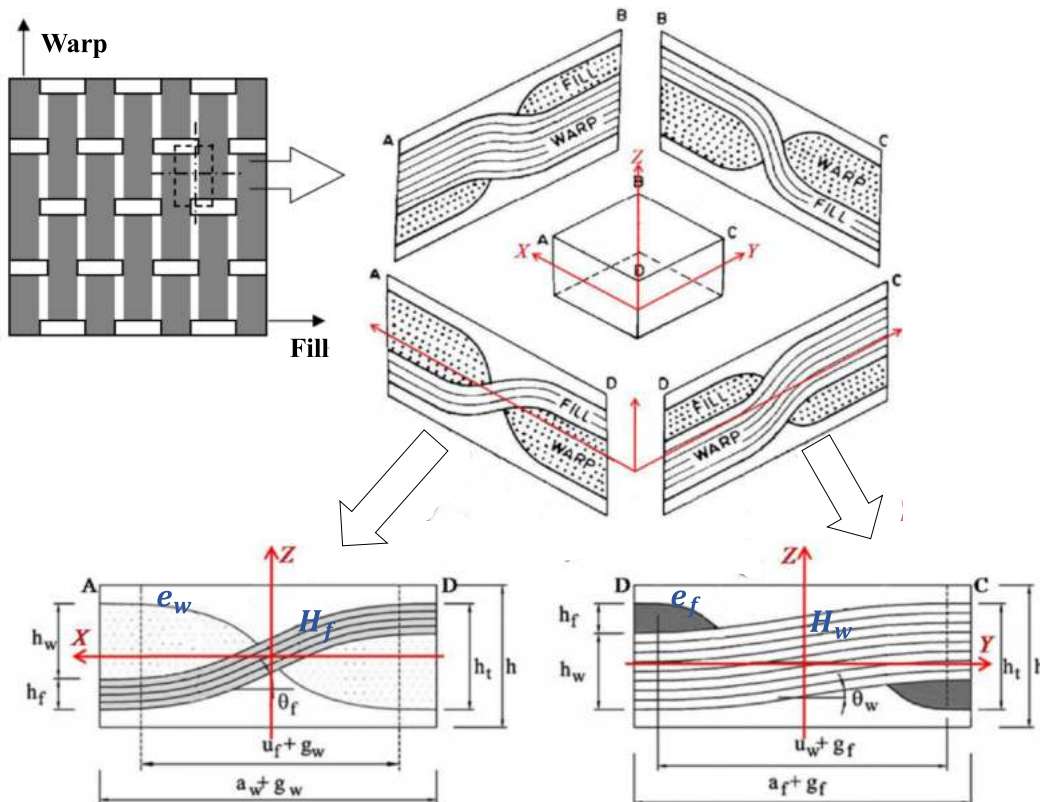
Fig. 3. The unit cell of the plain weave fabric composites.

Table 3
Geometric parameters for carbon/epoxy strands and the unit cell.

Dimension of the unit cell (mm)		Width of yarn (mm)		Gap between adjacent yarn (mm)		Thickness of yarn (mm)		Thickness of fabric (mm) h_t
Fill l_x	Warp l_y	Warp a_w	Fill a_f	Warp g_w	Fill g_f	Warp h_w	Fill h_f	
1.11	1.11	1.10	0.96	0.01	0.15	0.075	0.075	0.15

where,

$$\eta_2 = \frac{\frac{E_2^f}{E^m} - 1}{\frac{E_2^f}{E^m} + \xi} \tag{4}$$

The semi-empirical Halpin-Tsai relationship is also used to calculate the in-plane shear modulus G_{12}^s with the parameter $\xi = 2$ [40]:

$$G_{12}^s = \frac{G^m(1 + \xi\eta_{12}V_f^s)}{(1 - \eta_{12}V_f^s)} \tag{5}$$

where,

$$\eta_{12} = \frac{\frac{G_{12}^f}{E^m} - 1}{\frac{G_{12}^f}{E^m} + \xi} \tag{6}$$

The yarn is hypothesized transversely isotropic in the YZ plane, and the shear modulus in this plane G_{23}^s is:

$$G_{23}^s = \frac{E_2^s}{2(1 + \nu_{23}^s)} \tag{7}$$

The axial in-plane Poisson's ratio ν_{12}^s is predicted by the rule of mixture:

$$\nu_{12}^s = V_f^s\nu_{12}^f + (1 - V_f^s)\nu^m \tag{8}$$

The transverse in-plane Poisson's ratio ν_{21}^s is calculated by the reciprocity relationship:

$$\nu_{21}^s = \frac{E_2^s}{E_1^s}\nu_{12}^s \tag{9}$$

Then the out-of-plane Poisson's ratio ν_{23}^s is predicted by the rule of mixture:

$$\nu_{23}^s = V_f^s\nu_{23}^f + (1 - V_f^s)\nu^m \tag{10}$$

It can be seen from the unit cell of WF composites in Fig. 3 that along the thickness direction, there are resin matrix, warp (or fill) yarn, fill (or warp) yarn and resin matrix. In addition to the Kirchhoff hypothesis and the perfect bonding assumption of CLT, there are some assumptions used in this work. The undulated yarns are idealized as curved beams, of which the neutral axis path can be depicted by sinusoidal or cosinusoidal shape function. The cross-section of the fibre yarn remains unchanged

and is regarded as an ellipse. The geometric parameters based on the results measured by Naik et.al [41] using an optical microscope and processed by Sheng et. al [39] were obtained and listed in Table 3. Therein, l_x and l_y are the length and width of the unit cell, respectively. a_w and a_f denote the width of cross-sections of warp and fill yarns, respectively. h_w and h_f represent the thickness of cross-sections of warp and fill yarns, respectively. The above parameters are the same as the data in Reference [39]. The gap between adjacent warp and fill yarns g_w and g_f are calculated by:

$$\begin{cases} g_w = l_x - a_w \\ g_f = l_y - a_f \end{cases} \tag{11}$$

The thickness of WF fabric h_t is obtained by:

$$h_t = h_w + h_f \tag{12}$$

Affected by factors such as textile tension, width and thickness of the yarn, spacing distance between adjacent yarns, etc., the segment at the top or bottom of the fibre yarn may maintain straight in a small range. This can be seen in Fig. 3, in fill direction as $a_w - u_f$, and in warp direction as $a_f - u_w$. However, from a global perspective, the edges of undulated yarns and their vertical ellipse cross-sections are highly coincident. Thus, the undulation of warp and fill yarns u_w and u_f satisfy:

$$\begin{cases} u_w = a_f \\ u_f = a_w \end{cases} \tag{13}$$

It should be noted that the thickness of fabric is generally less than the thickness of laminates. The latter controls the fibre volume fraction for laminates with a specified number of layers, for instance, one layer here. Therefore, for the purpose of engineering application, attention is paid to the ply thickness of WF composites h, rather than the overall fibre volume fraction.

For the AD plane in Fig. 3, the centre of the fill yarn $H_f(x)$ can be expressed as:

$$H_f(x) = \begin{cases} h_w/2, & -(a_w + g_w)/2 \leq x \leq -(u_f + g_w)/2 \\ -h_w\sin[\pi x/(u_f + g_w)]/2, & -(u_f + g_w)/2 \leq x \leq (u_f + g_w)/2 \\ -h_w/2, & (u_f + g_w)/2 \leq x \leq (a_w + g_w)/2 \end{cases} \tag{14}$$

In this plane, the boundary of warp yarn that does not intersect with the fill yarn $e_w(x)$ is:

$$e_w(x) = \begin{cases} -h_t/2, & -(a_w + g_w)/2 \leq x \leq -(u_f + g_w)/2 \\ -\left[\frac{h_w}{2} - H_f\left(\frac{g_w}{2}\right)\right]\cos\left[\frac{\pi}{u_f}\left(x + \frac{u_f + g_w}{2}\right)\right] - H_f\left(\frac{g_w}{2}\right) - \frac{h_f}{2}, & -\frac{u_f + g_w}{2} \leq x \leq -\frac{g_w}{2} \\ \left[\frac{h_w}{2} - H_f\left(\frac{g_w}{2}\right)\right]\cos\left[\frac{\pi}{u_f}\left(x - \frac{u_f + g_w}{2}\right)\right] + H_f\left(\frac{g_w}{2}\right) + \frac{h_f}{2}, & \frac{g_w}{2} \leq x \leq \frac{u_f + g_w}{2} \\ h_t/2, & (u_f + g_w)/2 \leq x \leq (a_w + g_w)/2 \end{cases} \tag{15}$$

For the DC plane, the centre of the warp yarn $H_w(y)$ can be expressed as:

$$H_w(y) = \begin{cases} -h_f/2, & -(a_f + g_f)/2 \leq y \leq -(u_w + g_f)/2 \\ h_f \sin[\pi y/(u_w + g_f)]/2, & -(u_w + g_f)/2 \leq y \leq (u_w + g_f)/2 \\ h_f/2, & (u_w + g_f)/2 \leq y \leq (a_f + g_f)/2 \end{cases} \quad (16)$$

In this plane, the boundary of fill yarn that does not intersect with the warp yarn $e_f(y)$ is:

$$e_f(y) = \begin{cases} h_t/2, & -(a_f + g_f)/2 \leq y \leq -(u_w + g_f)/2 \\ \left[\dfrac{h_f}{2} + H_w\left(\dfrac{g_f}{2}\right)\right] \cos\left[\dfrac{\pi}{u_w}\left(y + \dfrac{u_w + g_f}{2}\right)\right] - H_w\left(\dfrac{g_f}{2}\right) + \dfrac{h_w}{2}, & -\dfrac{u_w + g_f}{2} \leq y \leq -\dfrac{g_f}{2} \\ -\left[\dfrac{h_f}{2} + H_w\left(\dfrac{g_f}{2}\right)\right] \cos\left[\dfrac{\pi}{u_w}\left(y - \dfrac{u_w + g_f}{2}\right)\right] + H_w\left(\dfrac{g_f}{2}\right) - \dfrac{h_w}{2}, & \dfrac{g_f}{2} \leq y \leq \dfrac{u_w + g_f}{2} \\ -h_t/2, & (u_w + g_f)/2 \leq y \leq (a_f + g_f)/2 \end{cases} \quad (17)$$

Local angels between the fill yarn and global X-axis $\theta_f(x)$, warp yarn and global Y-axis $\theta_w(y)$ are:

$$\begin{cases} \theta_f(x) = \tan^{-1}\left(\dfrac{dH_f(x)}{dx}\right) \\ \theta_w(y) = \tan^{-1}\left(\dfrac{dH_w(y)}{dy}\right) \end{cases} \quad (18)$$

The transformed stiffness matrix $\overline{Q}_{ij}^e$ is derived by:

$$\overline{Q}_{ij}^e = \left[T_{ij}^e\right]^{-1}\left[Q_{ij}^e\right]\left[R_{ij}\right]\left[T_{ij}^e\right]\left[R_{ij}\right]^{-1} \quad (19)$$

where superscript e can be any of w, f or m, representing the warp, fill yarns and pure matrix. $\overline{Q}_{ij}^e$ can be given by the corresponding stiffness matrix Q_{ij}^e and local angles of yarns. Therein, the Q_{ij}^e can be expressed by the relative elastic parameters of yarns and matrix as [42]:

$$Q_{ij}^e = \begin{bmatrix} Q_{11}^e & Q_{12}^e & Q_{13}^e & 0 & 0 & 0 \\ Q_{21}^e & Q_{22}^e & Q_{23}^e & 0 & 0 & 0 \\ Q_{31}^e & Q_{32}^e & Q_{33}^e & 0 & 0 & 0 \\ 0 & 0 & 0 & Q_{44}^e & 0 & 0 \\ 0 & 0 & 0 & 0 & Q_{55}^e & 0 \\ 0 & 0 & 0 & 0 & 0 & Q_{66}^e \end{bmatrix} \quad (20)$$

where,

$$Q_{11}^e = E_1^e \frac{1 - \vartheta_{23}^e \vartheta_{32}^e}{\Delta^e},$$

$$Q_{22}^e = E_2^e \frac{1 - \vartheta_{31}^e \vartheta_{13}^e}{\Delta^e},$$

$$Q_{33}^e = E_3^e \frac{1 - \vartheta_{12}^e \vartheta_{21}^e}{\Delta^e},$$

$$Q_{12}^e = Q_{21}^e = E_1^e \frac{\vartheta_{21}^e + \vartheta_{31}^e \vartheta_{12}^e}{\Delta^e},$$

$$Q_{13}^e = Q_{31}^e = E_1^e \frac{\vartheta_{31}^e + \vartheta_{21}^e \vartheta_{32}^e}{\Delta^e},$$

$$Q_{23}^e = Q_{32}^e = E_2^e \frac{\vartheta_{32}^e + \vartheta_{12}^e \vartheta_{31}^e}{\Delta^e},$$

$$Q_{44}^e = G_{23}^e,$$
$$Q_{55}^e = G_{13}^e,$$
$$Q_{66}^e = G_{12}^e,$$

$$\Delta^e = 1 - \vartheta_{12}^e \vartheta_{21}^e - \vartheta_{23}^e \vartheta_{32}^e - \vartheta_{31}^e \vartheta_{13}^e - 2\vartheta_{13}^e \vartheta_{21}^e \vartheta_{32}^e,$$
$$\frac{\vartheta_{ij}^e}{E_i^e} = \frac{\vartheta_{ji}^e}{E_j^e}.$$

The stiffness of the matrix Q_{ij}^m and warp yarn Q_{ij}^w, fill yarn Q_{ij}^f can be obtained by mechanical parameters of the matrix in Table 1 and fibre strands in Table 2. The R and T are the Reuter matrix and the global–local stress transformation matrix, respectively:

$$R_{ij} = \begin{bmatrix} 1 & 0 & 0 & 0 & 0 & 0 \\ 0 & 1 & 0 & 0 & 0 & 0 \\ 0 & 0 & 1 & 0 & 0 & 0 \\ 0 & 0 & 0 & 2 & 0 & 0 \\ 0 & 0 & 0 & 0 & 2 & 0 \\ 0 & 0 & 0 & 0 & 0 & 2 \end{bmatrix} \quad (21)$$

$$T_{ij}^w = \begin{bmatrix} 0 & c_w^2 & s_w^2 & 2c_w s_w & 0 & 0 \\ 1 & 0 & 0 & 0 & 0 & 0 \\ 0 & s_w^2 & c_w^2 & -c_w s_w & 0 & 0 \\ 0 & 0 & 0 & 0 & c_w & s_w \\ 0 & -c_w s_w & c_w s_w & c_w^2 - s_w^2 & 0 & 0 \\ 0 & 0 & 0 & 0 & s_w & c_w \end{bmatrix} \quad (22)$$

$$T_{ij}^f = \begin{bmatrix} c_f^2 & 0 & s_f^2 & 0 & 2c_f s_f & 0 \\ 0 & 1 & 0 & 0 & 0 & 0 \\ s_f^2 & 0 & c_f^2 & 0 & -2c_f s_f & 0 \\ 0 & 0 & 0 & c_w & 0 & -s_f \\ -c_f s_f & 0 & c_f s_f & 0 & c_f^2 - s_f^2 & 0 \\ 0 & 0 & 0 & s_f & 0 & c_f \end{bmatrix} \quad (23)$$

where $s_w = \sin\theta_w, c_w = \cos\theta_w, s_f = \sin\theta_f, c_f = \cos\theta_f$. After the fabric geometry is defined, CLT can be applied to determine the effective material constants, which can be expressed as [43]:

$$\begin{Bmatrix} N_i \\ M_i \end{Bmatrix} = \begin{bmatrix} A_{ij}(x,y) & B_{ij}(x,y) \\ B_{ij}(x,y) & D_{ij}(x,y) \end{bmatrix} \begin{Bmatrix} \varepsilon_j^0 \\ \kappa_j \end{Bmatrix} \quad (24)$$

where N_i, M_i denote the membrane stress and moment resultants, respectively. ε_j^0, κ_j represent strain and curvature of the neutral surface. The in-plain stiffness matrices are given by:

$$\{A_{ij}(x,y), B_{ij}(x,y), D_{ij}(x,y)\} = \int_{-h/2}^{h/2} (1, z, z^2)\overline{Q}_{ij}^e dz \quad (25)$$

For the region of $-(u_w + g_w)/2 < x < 0 \,\&\, -(u_f + g_f)/2 < y < 0$, these

Table 4
Fabric specifications and mechanical properties for validation.

Parameters	E-glass/epoxy [44]	E-glass/epoxy [39]	T300/epoxy [39]
$l_x = l_y$(mm)	0.67	0.73	1.11
$a_w = a_f$(mm)	0.62	0.5	1.1
$g_w = g_f$(mm)	0.05	0.23	0.01
$h_w = h_f$(mm)	0.1	0.05	0.075
h(mm)	0.21	0.15	0.16
E_1^s(GPa)	51.5	51.1	148.8
$E_2^s = E_3^s$(GPa)	17.5	16	12.2
G_{12}^s(GPa) G_{13}^s(GPa)	5.8	5.77	4.81
G_{23}^s(GPa)	6.68	6.11	4.73
$\nu_{21}^s = \nu_{31}^s$	0.105	0.096	0.024
ν_{23}^s	0.31	0.31	0.29
V_f^s	0.7	0.7	0.64
E_m(GPa)	3.5	3.5	3.5
G_m(GPa)	1.3	1.3	1.3
ν_m	0.35	0.35	0.35

the stiffness constants $\overline{A}_{ij}^s(y), \overline{B}_{ij}^s(y), \overline{D}_{ij}^s(y)$ are obtained. Next, the average in-plain stiffness terms of the whole unit cell are found by integrating the stiffness mentioned above along the Y-axis:

$$\overline{A}_{ij}^{sp}, \overline{B}_{ij}^{sp}, \overline{D}_{ij}^{sp} = \frac{1}{a_f + g_f}\int_{-\frac{a_f+g_f}{2}}^{\frac{a_f+g_f}{2}} \overline{A}_{ij}^s(y), \overline{B}_{ij}^s(y), \overline{D}_{ij}^s(y)dy \tag{29}$$

Here the $\overline{A}_{ij}^{sp}, \overline{B}_{ij}^{sp}, \overline{D}_{ij}^{sp}$ matrices represent the average in-plane stiffness constants within the whole unit cell. The average in-plane compliance constants can be obtained by inverting $\overline{A}_{ij}^{sp}$ to $\overline{a}_{ij}^{sp}$. After that, in conjunction with the following equations [35], the effective elastic constants can be derived as:

stiffness matrices can be derived as:

$$\begin{aligned}
A_{ij}(x,y), B_{ij}(x,y), D_{ij}(x,y) = &\int_{-h/2}^{H_w(y)-t_w(x)}(1,z,z^2)\left[\overline{Q}_{ij}^m\right]dz + \int_{H_w(y)-t_w(x)}^{H_w(y)+t_w(x)}(1,z,z^2)\left[\overline{Q}_{ij}^w\right]dz + \int_{H_f(x)-t_f(y)}^{H_f(x)+t_f(y)}(1,z,z^2)\left[\overline{Q}_{ij}^f\right]dz + \int_{H_f(x)+t_f(y)}^{h/2}(1,z,z^2)\left[\overline{Q}_{ij}^m\right]dz \\
&+ \int_{-h/2}^{H_f(x)-h_f/2}(1,z,z^2)\left[\overline{Q}_{ij}^m\right]dz + \int_{H_f(x)-h_f/2}^{H_f(x)+h_f/2}(1,z,z^2)\left[\overline{Q}_{ij}^f\right]dz + \int_{H_f(x)+h_f/2}^{h/2}(1,z,z^2)\left[\overline{Q}_{ij}^m\right]dz + \int_{-h/2}^{H_w(y)-h_w/2}(1,z,z^2)\left[\overline{Q}_{ij}^m\right]dz \\
&+ \int_{H_w(y)-h_w/2}^{H_w(y)+h_w/2}(1,z,z^2)\left[\overline{Q}_{ij}^w\right]dz + \int_{H_w(y)+h_w/2}^{h/2}(1,z,z^2)\left[\overline{Q}_{ij}^m\right]dz + \int_{-h/2}^{h/2}(1,z,z^2)\left[\overline{Q}_{ij}^m\right]dz
\end{aligned} \tag{26}$$

where,

$$\begin{cases} t_w(x) = \left[H_f(x) - h_f/2 - e_w(x)\right]/2 \\ t_f(y) = \left[e_f(y) - H_w(y) - h_w/2\right]/2 \end{cases} \tag{27}$$

After that, the Series-Parallel (SP) model is used to average stiffness terms within the unit cell [35]. Firstly, the compliance matrices $a_{ij}(x,y)$, $b_{ij}(x,y), d_{ij}(x,y)$ can be obtained by inverting the stiffness terms $A_{ij}(x,y)$, $B_{ij}(x,y), D_{ij}(x,y)$. The in-plane compliance matrices along X-axis can be written as:

$$\overline{a}_{ij}^s(y), \overline{b}_{ij}^s(y), \overline{d}_{ij}^s(y) = \frac{1}{a_w + g_w}\int_{-\frac{a_w+g_w}{2}}^{\frac{a_w+g_w}{2}} a_{ij}(x,y), b_{ij}(x,y), d_{ij}(x,y)dx \tag{28}$$

Then, by inverting the average compliance terms $\overline{a}_{ij}^s(y), \overline{b}_{ij}^s(y), \overline{d}_{ij}^s(y)$,

$$\begin{cases} E_x = \dfrac{1}{\overline{a}_{11}^{sp}h} \\[2mm] E_y = \dfrac{1}{\overline{a}_{22}^{sp}h}, \\[2mm] E_z = \dfrac{1}{\overline{a}_{33}^{sp}h} \end{cases} \begin{cases} G_{yz} = \dfrac{1}{\overline{a}_{44}^{sp}h} \\[2mm] G_{zx} = \dfrac{1}{\overline{a}_{55}^{sp}h}, \\[2mm] G_{xy} = \dfrac{1}{\overline{a}_{66}^{sp}h} \end{cases} \begin{cases} \nu_{xy} = -\dfrac{\overline{a}_{12}^{sp}}{\overline{a}_{11}^{sp}} \\[2mm] \nu_{xz} = -\dfrac{\overline{a}_{13}^{sp}}{\overline{a}_{11}^{sp}} \\[2mm] \nu_{yz} = -\dfrac{\overline{a}_{23}^{sp}}{\overline{a}_{22}^{sp}} \end{cases} \tag{30}$$

There are three sets of experimental results from the literature [39,44] in Table 5 to validate the model. The fabric geometric specifications and mechanical properties are listed in Table 4. The mosaic model [45], one-dimensional (1D) undulation model [46], two-dimensional parallel-series (2D PS) model [35], two-dimensional

Table 5
Tensile modulus from experimental results and predicted data from different models.

Models	E-glass/epoxy		E-glass/epoxy		T300/epoxy	
	Prediction	Error (%)	Prediction	Error (%)	Prediction	Error (%)
Experiments	19.3 [44]		14.5 [39]		60.3 [39]	
Mosaic model [45]	19.71	+2.1	12.89	−11.1	54.82	−9.1
1D model [46]	16.18	−16.2	12.39	−14.6	44.70	−25.9
2D PS model [35]	19.12	−0.9	11.89	−18.0	47.04	−22.0
2D SP model [35]	19.08	−1.1	11.82	−18.5	47.03	−22.0
Curved beam model [47]	19.09	−1.1	13.41	−7.5	58.91	−2.3
Present work	20.26	+4.97	14.38	−0.03	50.37	−16.47

Table 6
Variation of tensile modulus with the laminate thickness.

Laminate thickness h (mm)	0.2	0.3	0.4	0.5	0.6	0.7	0.8	0.9	1.0
Tensile modulus $E_x^{45°}$ (GPa)	7.16	6.35	5.91	5.63	5.43	5.27	5.15	5.05	4.97
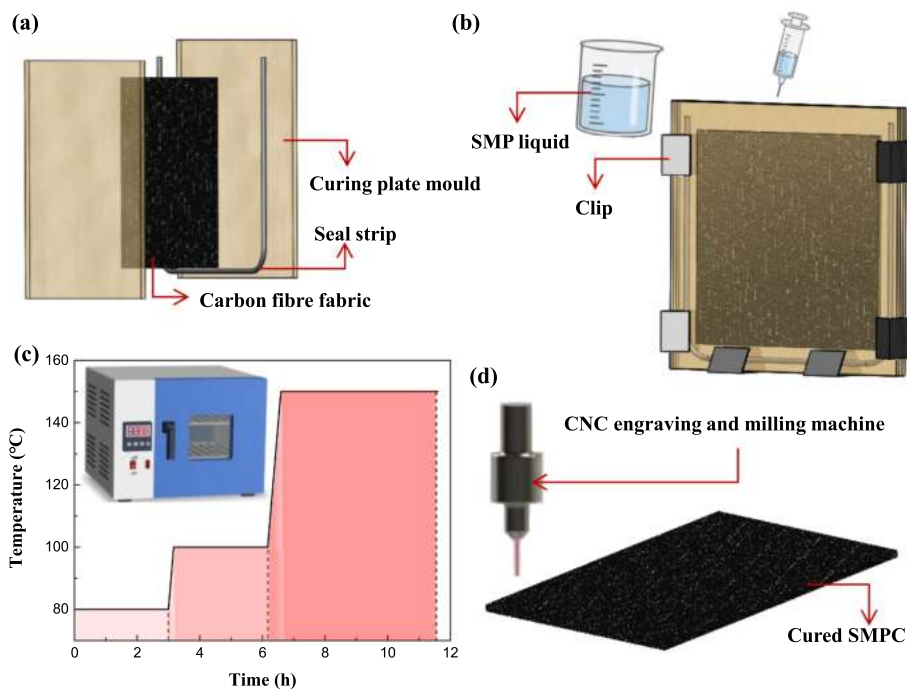
Fig. 4. Preparation of the SMPC specimens, (a) the curing mould, (b) polymer infusion method, (c) curing process and (d) cured SMPC cut by a CNC machine.

series–parallel (2D SP) model [35], modified curved beam model [47] and the model used in this work are applied to conduct the prediction in Table 5. In fact, all mosaic, 1D, 2D PS, 2D SP models and the model used in this work are derived from the CLT. They neglect the interaction between the orthogonal interlacing yarns. Whereas the modified beam model adopted a strain energy approach which accounted for both the interaction between orthogonal interlacing yarns and the undulation of warp or fill yarns. Xiong et.al [47] has pointed out that the tensile modulus is governed by the coupling effect of the interaction between orthogonal interlacing yarns and the undulation of warp or fill yarns. The former would cause an increase while the latter should lead to a decrease in the tensile modulus. In fact, experimental results are also affected by the sample preparation technique, experimental methods, and data processing approach etc. Overall, the model used in this work can produce valid and rational results, and can be used to design the SMPC device.

For composites with an orientation of ± 45° used in SMPC devices, the tensile modulus $E_x^{45°}$ can be derived as:

$$\frac{1}{E_x^{45°}} = \frac{1}{E_x}cos^4 45° + \left(\frac{1}{G_{xy}} - \frac{2\nu_{yx}}{E_x}\right)sin^2 45° cos^2 45° + \frac{1}{E_y}sin^4 45° \tag{31}$$

The tensile modulus of laminates oriented at ± 45° with different thicknesses is listed in Table 6. It is in line with common sense that the tensile modulus decreases with laminate thickness, and the decrease rate slows down. The tensile modulus is required greater than 5 GPa. However, results with thicknesses from 0.2 mm to 0.9 mm all fulfil this requirement. Therefore, we must further consider the fabrication technique, shape moulding and weight reduction demands.

The preparation of SMPC specimens is illustrated in Fig. 4. The
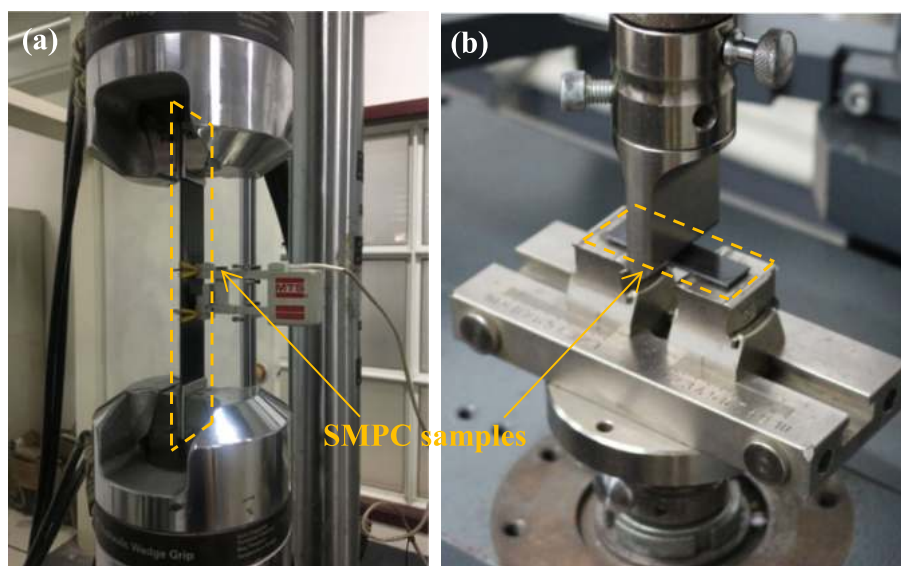
Fig. 5. Experimental setup for (a) tensile tests and (b) three-point bending tests.
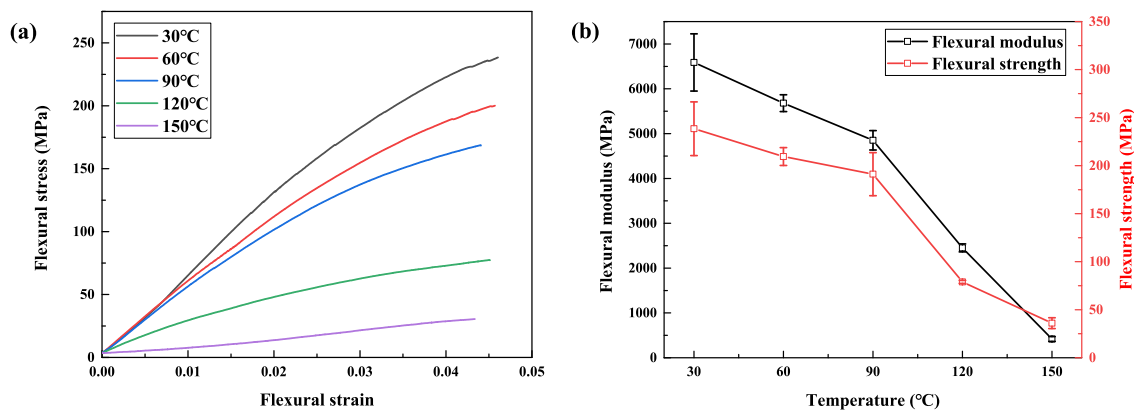
Fig. 6. Three-point bending results of SMPC, (a) flexural stress versus strain curves and (b) flexural modulus and flexural strength versus temperature curves.

curing mould in Fig. 4 (a) is composed of two glass plates with release fabrics attached to their surfaces. These two slides are separated by a seal strip, which can also be used to control the thickness of samples. The carbon fabric sheets were layered in the predetermined orientation (±45° along the axis). The detailed composition of the epoxy based SMP is proprietary to our lab. It consists of an epoxy base resin, a hardener and a linear monomer. The mixture was degassed in a vacuum oven at 50 °C for 30 min before being injected into the mould. The pre-polymer infusion in Fig. 4 (b) can be assisted by a syringe or other tools. Then, a three-step curing process in Fig. 4 (c) was carried out in an oven at 80 °C for 3 h, 100 °C for 3 h and 150 °C for 5 h, with a heating rate of 2 °C/min. The cured composites were naturally cooled to room temperature and then demoulded. Finally, the specimens with the required dimensions were obtained by a computer-numerical-controlled (CNC) engraving and milling machine in Fig. 4 (d).

To obtain composites with less imperfection, for instance, void, the minimum thickness of composites made by this polymer infusion technique is 0.4 mm, empirically. In addition, the imperfection and lower matrix fraction will weaken the shape memory performance for thinner laminates. On the other hand, thicker laminate shows a smaller elastic modulus and is not conducive to bending deformation or weight reduction purposes. Therefore, the laminate thickness is 0.4 mm for a balance between mechanical requirements and material preparation.

The flat SMPC release device was cut into a dimension of 104 mm in length, 25 mm in width and drilled with two holes (diameter of 2 mm) for instalment. It is designed to deform with a bending angle of 300° and radius of 13.5 mm, suitable for latching components in cylinder shapes. The bending angle of 300° contributes to improving the mechanical response of the mechanism, while also posing a challenge to shape moulding and long-term shape fixation. The apparatus for shape

moulding in Fig. 1 (c) comprises an internal mould, an external mould and a clamp. The internal mould is a cylinder featured in a radius of 13 mm, which is 0.5 mm smaller than the radius of the SMPC device because elastic recovery is inevitable during shape moulding. A plate protrudes from its tangent direction with two holes for installing SMPC plates. The external mould consists of three parts. The external mould-1 is a plate and a ring with a central angle of 120°. The external mould-2 is the same ring with an arc angle of 180°. These two parts are joined together by a pin (external mould-3), providing a rotational degree of freedom. The clamp is used to maintain deformation. The profile of the shaped device is portrayed in yellow dashed lines. The shape moulding process could be divided into three steps: deformation at high temperatures, maintaining deformation while cooling, and unloading at low temperatures. Firstly, the flat SMPC device was fixed on the internal mould and put into a 170 °C oven for 20 min. Then, the straight portion of external mould-1 was put on the specimen tightly, and the external mould-2 was rotated to complete a large-angle bending. Next, the clamp was screwed to maintain the deformation, and the whole structure was cooled down to room temperature. Finally, the shaped SMPC device was obtained when the clamp was removed.

The recovery of the SMPC device is stimulated by a resistor heater (25 Ω) that elevates the temperature when powered. Two adhesion methods and corresponding infrared thermal images are shown in Fig. 1 (d) and (e), respectively. For simple adhesion, the resistor heater is fixed on the outer surface of SMPC devices by PI tape. The infrared image shows 188.92 °C on the outer surface and 141.75 °C on the inner surface. Although according to DMA results (in Fig. 2), it is sufficient to drive shape memory recovery, the temperature difference of 47.17 °C is not conducive to prolonging the service life. Therefore, adhesion is modified by adding two layers of Al tape between the SMPC and heater, heater
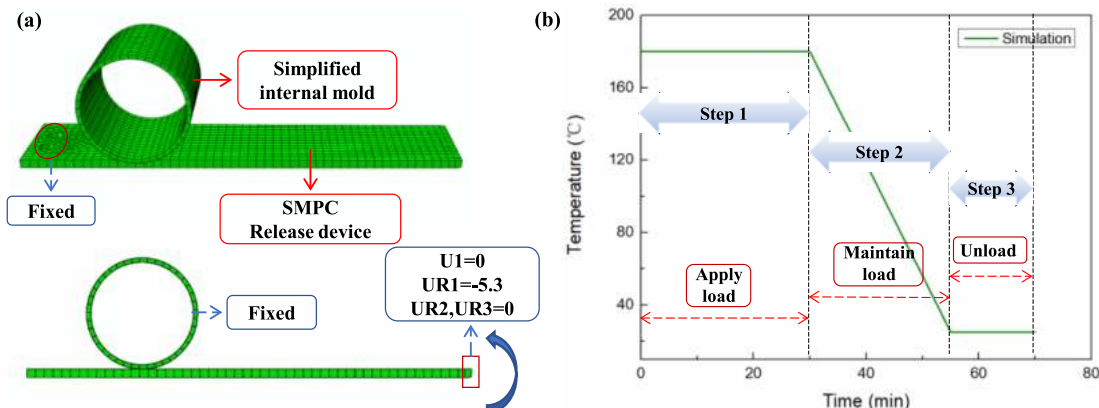
Fig. 7. Simulation of shape memory effect, (a) finite element model and (b) temperature and load details.
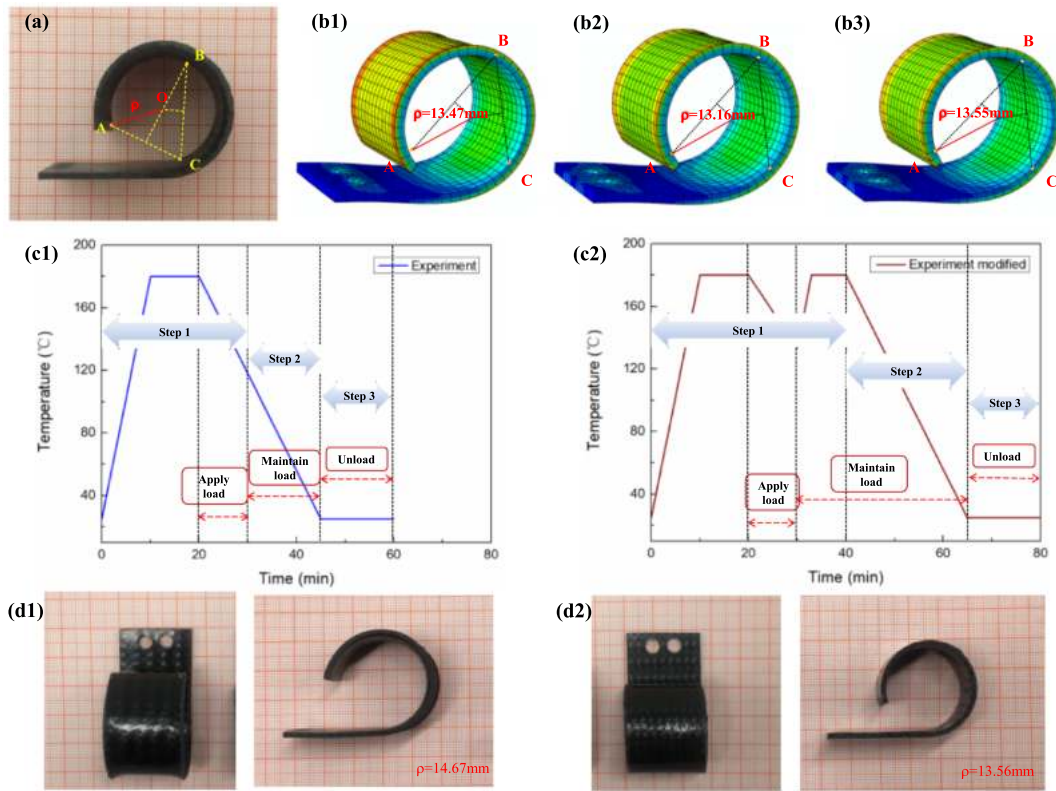
Fig. 8. SMPC devices in shaped configurations, (a) experimental radius of curvature, (b) curvatures from simulation after (b1) step 1, (b2) step 2 and (b3) step 3, (c) experimental temperature and load details for (c1) original and (c2) modified moulding methods, (d) shaped SMPC devices from (d1) original and (d2) modified moulding methods.

and PI tape, resulting in 169.70 ℃ on the outer surface and 150.46 ℃ on the inner surface. The temperature difference along the thickness is reduced to 19.24 ℃. Although the addition of Al tape reduces the maximum temperature, it contributes to a more uniform thermal distribution inside the SMPC, facilitating both shape recovery and reusability. Finally, the papyrus scroll mechanism is assembled and fixed on a platform in Fig. 1 (b), and heaters are connected to the power supply for triggering deployments.

2.3. Mechanical experiments of SMPC specimens

2.3.1. Tensile tests

Static tensile tests were conducted at room temperature in Fig. 5 (a) where specimens were prepared following the standard ASTM D3039 with a dimension of 250 mm × 25 mm. These coupons were stretched by a uni-axial MTS servo-hydraulic testing machine (C45.105) with a load cell of 100 kN and a preload of 10 N at a tensile rate of 2 mm/min until broken. The tensile modulus is identified as the slope of the initial straight line of stress–strain curves. The average value from tests is 5.42 GPa, higher than the required 5 GPa, but shows an 8.29 % decrease from the theoretical result of 5.91 GPa in Table 6. The discrepancy is inevitable and acceptable due to experimental errors, preparation defects and simplification of theoretical models.

2.3.2. Three-point bending tests

Bending is the dominant deformation form of SMPCs in this mechanism. Therefore, three-point bending tests in Fig. 5 (b) were carried out on a Zwick/Rolle 010 testing machine with a temperature chamber at five temperatures (30 ℃, 60 ℃, 90 ℃, 120 ℃ and 150 ℃) and at least three specimens for each group. These specimens were cut according to the standard ASTM D790 with 12.7 mm in width and 60 mm in length. The support span-thickness ratio was set to be 16:1. These samples were

first heated to the target temperature at a heating rate of 3 ℃/min and then left at that temperature for 20 min to ensure a completely uniform thermal distribution. Subsequently, a preload of 2 N at a crosshead velocity of 2 mm/min was performed. The bending tests were conducted at 1 mm/min and terminated when the deflection of 5 mm was reached or the specimen was broken before that. The flexural stress σ_f, flexural strain ε_f and flexural modulus E_f can be calculated as:

$$\sigma_f = \frac{3FL}{2bd^3} \tag{32}$$

$$\varepsilon_f = \frac{6Dd}{L^2} \tag{33}$$

$$E_f = \frac{mL^3}{4bd^3} \tag{34}$$

In these equations, F is the load, L represents the support span, b and d are the specimens' width and thickness, respectively. D is the maximum deflection which is also the displacement of the crosshead, and m is the slope of the initial straight line of the load–deflection curves. Specimens tested at all temperatures exhibit no crack or failure within 5 mm deflection. The flexural stress versus strain at five temperatures is shown in Fig. 6 (a). The SMPC shows a stiffening response at 30 ℃, 60 ℃ and 90 ℃ under bending with no crack observed. With the elevation of temperature, the material yields. The flexural modulus and strength in Fig. 6 (b) show a rapid decrease above 90 ℃. These temperatures are close to or above the T_g (144 ℃), at which the epoxy matrix gets soft from the glassy to the rubbery state, showing good agreement with DMA results in Fig. 2. The flexural modulus and strength decrease from about 6580 MPa to 418 MPa and 226 MPa to 36 MPa, respectively, showing an order of magnitude drop.
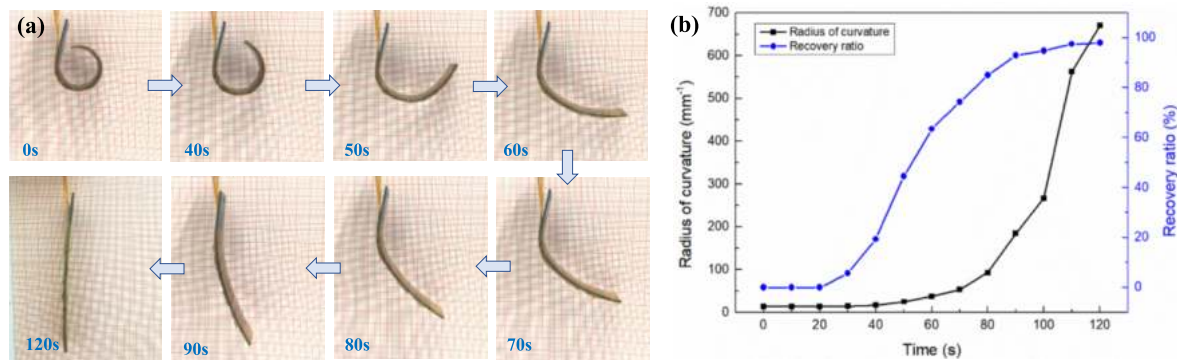
Fig. 9. Shape memory recovery of SMPC release devices stimulated by 28 V DC voltage, (a) the recovery process and (b) radius of curvature and recovery ratio versus time curves.

2.4. Shape memory characteristics of the SMPC device

The reliable locking and self-deployment of the papyrus scroll mechanism rely on the shape memory fixation and recovery properties of SMPC devices, respectively. Therefore, these two properties will be investigated from the perspective of numerical simulation and experimental verification. Firstly, a finite element model in Fig. 7 (a) consisting of a flat SMPC specimen and simplified internal mould (a tube with an outer diameter of 13 mm and thickness of 1 mm) was created. For material parameters of the SMPC, the elastic modulus was obtained from tensile tests, Poisson's ratio and viscoelastic parameters were adopted from the literature [34] where the matrix was from the same epoxy system. Four "Visco" steps were used to simulate the shape memory effect. They were set as: (i) deformation at high temperatures, (ii) maintaining load while cooling, (iii) unloading at low temperatures and (iv) heating to recovery. The SMPC specimen was meshed using the "Structured" technique, forming 693 C3D20 elements. The fixed boundary condition was applied to two holes on the SMPC and internal mould, while the rotation was applied to the node set on the right side. The surface-to-surface contact was assigned by specifying the outer surface of the mould as the master surface and the upper surface of SMPC as the slave surface.

As for the experimental section, the recovery tests were conducted with a paper as the background, on which the length of the smallest square was 1 mm. With these squares, the radius of curvature was easy to measure from the recovery pictures. The measurement method was illustrated in Fig. 8 (a), where point A was located at 2 mm from the free end, point C was 35 mm away from the fixed end, and point B was positioned at the intersection of the line AC perpendicular bisector and the arc. The centre of the circle (point O) was at the intersection of lines AC and BC perpendicular bisectors. Thus, the radius of curvature was obtained as the length of line OA (or OB or OC). The recovery ratio R_t is calculated as:

$$R_t = \frac{1/\rho_0 - 1/\rho_t}{1/\rho_0} \times 100\% \tag{35}$$

here ρ is the radius of curvature, and ρ_0 represents the initial radius and ρ_t is the radius when recovery time is t.

2.4.1. Shape fixation properties

The temperature and load details of the numerical simulation are described in Fig. 7 (b) where the heating rate of 15 ℃/min and cooling rate of 6 ℃/min are set. The configurations of the shaped SMPC device after the first three steps are shown in Fig. 8 (b1) to (b3). Because of the inaccuracy and difficulty in measuring the bending angle, which is a common parameter for shape fixation assessment, the radius of curvature is proposed for easy measurements. The numbers 73, 88 and 103 nodes denoted as points A, B and C, respectively, are selected to calculate the radius of curvature ρ, the same as those in experiments in Fig. 8

(a). It turns out to be 13.47 mm, 13.16 mm and 13.55 mm after step 1, step 2 and step 3, respectively. The thermal expansion effect causes the decrease of radius after step 2, and the increase after step 3 is because of the elastic recovery. The radius shows little difference from the designed one.

Conversely, there are some differences in temperature and load details between the simulation and experiments. The discrepancy focuses on step 1, where the deformation is created under constant high temperatures in simulation (Fig. 7 (b)), while it suffers a cooling period in practical operation (Fig. 8 (c1)). This cooling period causes difficulty in shape moulding because the stiffness increases significantly, and results in an unexpected but apparent elastic recovery. A reheating and sustaining high-temperature period is added after step 1 (modified moulding method), as shown in Fig. 8 (c2), to obtain a more accurate configuration. Compared with the previous process in Fig. 8 (c1), the modified method results in a similar moulding scheme as the simulation. Curved SMPC devices obtained from two moulding methods are shown in Fig. 8 (d1) and (d2), respectively. From the front view, the device obtained from the original method has an obvious saddle surface, while the modified technique produces a smoother surface. From the side view, the original one deviates from the designed circle, and the radius of curvature is significantly larger than that of the simulation. The modified one shows good consistency with the results shown in Fig. 8 (b3). It suggests that the modified moulding method contributes to desired shapes.

2.4.2. Shape recovery properties

The shape memory recovery of SMPC devices driven by 28 V DC voltage under normal temperature (about 25 ℃) and pressure (about 101.35 KPa) is shown in Fig. 9. It maintains intact in the first 40 s and follows a rapid recovery from 40 s to 90 s. The recovery becomes slow in the late 30 s and finishes at 120 s with a recovery ratio of 97.93 %, which is less than the value (99.89 %) obtained from the simulation. This may be caused by two reasons. On the one hand, the SMPC is restricted by adhesive tape because the intersection of tapes on the inner surface constrains its stretch. On the other, the local heating (region affixed with a resistor heater) results in a relatively low temperature at the margin (Fig. 1(e)). While in numerical simulation, the entire field and even the surrounding air are at a high temperature. However, fortunately, both simulation and experiment results are higher than 97 %, showing satisfactory recovery performance. The recovery of the mechanism and demonstration of the flag on Mars can be found in our previous work [28].

3. Conclusions

Compared with the existing flag demonstration scheme (pasted on the landing platform) in deep space explorations, the mechanism presents a dynamic demonstration, allowing the flag to flutter in the Martin

wind. This work focuses on the structural and material design, as well as the preparation process. Several conclusions can be drawn. Firstly, an ancient papyrus scroll-inspired mechanism is proposed to deploy the Chinese national flag in the Mars exploration mission. Then, SMPC devices, as a vital part of this self-deployable structure, are analysed. The orientation of carbon fibre fabric is designed empirically to be $\pm 45°$. As the yarn undulation in woven fabric composites weakens the in-plane stiffness, the laminate thickness is determined to be 0.4 mm through a theoretical model considering both mechanical and preparation requirements. The theoretical prediction is then verified by tensile tests. Additionally, the shape memory effect is analysed by both simulation and experiments. The moulding method is modified by adding a reheating and high-temperature period after applying load to realize the designed shape. As for shape recovery, both simulation and experiments demonstrate a recovery ratio greater than 97 %, showing the feasibility of reliable deployments. These smart materials and structures will play a vital role in the following Mars sample return and other deep space exploration missions.

Declaration of Competing Interest

The authors declare that they have no known competing financial interests or personal relationships that could have appeared to influence the work reported in this paper.

Data availability

Data will be made available on request.

Acknowledgements

References

[1] Sun Z. Technologies for Deep Space Exploration. Springer; 2021.
[2] Zheng Y. Mars Exploration in 2020. The Innovation 2020;1:100036.
[3] Wadhi MA, Bonnici M, Handley W. Pointing and Alignment for the Emirates Mars Mission. 2021 IEEE Aerospace Conference. Big Sky, MT, USA: IEEE; 2021. p. 1-8.
[4] Zou Y, Zhu Y, Bai Y, Wang L, Jia Y, Shen W, et al. Scientific objectives and payloads of Tianwen-1, China's first Mars exploration mission. Adv Space Res 2021;67: 812–23.
[5] Farley KA, Williford KH, Stack KM, Bhartia R, Chen A, de la Torre M, et al. Mars 2020 mission overview. Space Sci Rev 2020;216:1–41.
[6] Taylor EJ, Jackson GS. Perseverance Rover Lands on Mars. The Electrochemical Society Interface 2021;30:79.
[7] Hassler DM, Zeitlin C, Wimmer-Schweingruber RF, Ehresmann B, Rafkin S, Eigenbrode JL, et al. Mars' surface radiation environment measured with the Mars Science Laboratory's Curiosity rover. Science 2014;343:1244797.
[8] Li Y, Xiao Y, Yu L, Ji K, Li D. A review on the tooling technologies for composites manufacturing of aerospace structures: Materials, structures and processes. Compos A Appl Sci Manuf 2021;154:106762.
[9] Asyraf M, Ilyas R, Sapuan S, Harussani M, Hariz H, Aiman J, et al. Advanced Composite in Aerospace Applications: Opportunities, Challenges, and Future Perspective. Advanced Composites in Aerospace Engineering Applications 2022: 471–98.
[10] Nelyub V, Malysheva G. Modern treatment technologies of carbon fibre for ensuring the high strength carbon fibre reinforced plastic production. MATEC Web of Conferences: EDP Sciences 2017:02001.
[11] Hegde S, Shenoy BS, Chethan K. Review on carbon fiber reinforced polymer (CFRP) and their mechanical performance. Mater Today: Proc 2019;19:658–62.
[12] Zheng H, Zhang W, Li B, Zhu J, Wang C, Song G, et al. Recent advances of interphases in carbon fiber-reinforced polymer composites: a review. Compos B Eng 2022;233:109639.
[13] Liu T-W, Bai J-B. Folding behaviour of a deployable composite cabin for space habitats-Part 1: Experimental and numerical investigation. Compos Struct 2022; 302:116244.
[14] Liu T-W, Bai J-B. Folding behaviour of a deployable composite cabin for space habitats–Part 2: Analytical investigation. Compos Struct 2022;297:115929.
[15] Bahl S, Nagar H, Singh I, Sehgal S. Smart materials types, properties and applications: A review. Mater Today: Proc 2020;28:1302–6.
[16] Basheer AA. Advances in the smart materials applications in the aerospace industries. Aircraft Engineering and Aerospace Technology 2020;92:1027–35.
[17] Liu T, Zhou T, Yao Y, Zhang F, Liu L, Liu Y, et al. Stimulus methods of multi-functional shape memory polymer nanocomposites: A review. Compos A Appl Sci Manuf 2017;100:20–30.
[18] Liu T, Liu L, Yu M, Li Q, Zeng C, Lan X, et al. Integrative hinge based on shape memory polymer composites: Material, design, properties and application. Compos Struct 2018;206:164–76.
[19] Wei HQ, Liu LW, Zhang ZC, Du HY, Liu YJ, Leng JS. Design and analysis of smart release devices based on shape memory polymer composites. Compos Struct 2015; 133:642–51.
[20] Zhao H, Lan X, Liu L, Liu Y, Leng J. Design and analysis of shockless smart releasing device based on shape memory polymer composites. Compos Struct 2019;223: 110958.
[21] Li F, Liu L, Xin L, Zhou X, Bian W, Liu Y, et al. Preliminary design and analysis of a cubic deployable support structure based on shape memory polymer composite. International Journal of Smart and Nano Materials 2016;7:106–18.
[22] Zhang D, Liu L, Leng J, Liu Y. Ultra-light release device integrated with screen-printed heaters for CubeSat's deployable solar arrays. Compos Struct 2020;232: 111561.
[23] Zhang D, Liu L, Lan X, Leng J, Liu Y. Synchronous deployed design concept triggered by carbon fibre reinforced shape memory polymer composites. Compos Struct 2022;290:115513.
[24] Dixit A, Mali HS. Modeling techniques for predicting the mechanical properties of woven-fabric textile composites: a review. Mech Compos Mater 2013;49:1–20.
[25] Younes R, Hallal A, Fardoun F, Chehade FH. Comparative review study on elastic properties modeling for unidirectional composite materials. In: Hu N, editor. Composites and their properties. Rijeka, Croatia: Intech; 2012. p. 391–408.
[26] Ichihashi H, Hamada H, Ikuta N, Maekawa Z. Finite element analysis of woven fabric composites considering interfacial properties. Compos Interfaces 1994;2: 81–94.
[27] Yang J-M, Ma C-L, Chou T-W. Fiber inclination model of three-dimensional textile structural composites. J Compos Mater 1986;20:472–84.
[28] Dou Z, Liu Liwu Xu, Pengfei ZY, Qifeng Li, Xin L, et al. World's first application of a self-deployable mechanism based on shape memory polymer composites in Mars explorations: ground-based validation and on-Mars qualification. Smart Mater Struct 2022;31:115008. https://doi.org/10.1088/1361-665X/ac93d1.
[29] Li C, Liu J, Ren X, Zuo W, Tan X, Wen W, et al. The Chang'e 3 mission overview. Space Sci Rev 2015;190:85–101.
[30] Gierasch P, Sagan C. A preliminary assessment of Martian wind regimes. Icarus 1971;14:312–8.
[31] Leng J, Wu X, Liu Y. Effect of a linear monomer on the thermomechanical properties of epoxy shape-memory polymer. Smart Mater Struct 2009;18:095031.
[32] Li F, Liu L, Lan X, Pan C, Liu Y, Leng J, et al. Ground and geostationary orbital qualification of a sunlight-stimulated substrate based on shape memory polymer composite. Smart Mater Struct 2019;28:075023.
[33] Lan X, Liu L, Zhang F, Liu Z, Wang L, Li Q, et al. World's first spaceflight on-orbit demonstration of a flexible solar array system based on shape memory polymer composites. Science China Technological Sciences 2020;63:1436–51.
[34] Chen J, Liu L, Liu Y, Leng J. Thermoviscoelastic shape memory behavior for epoxy-shape memory polymer. Smart Mater Struct 2014;23:055025.
[35] Naik N, Shembekar P. Elastic behavior of woven fabric composites: I—Lamina analysis. J Compos Mater 1992;26:2196–225.
[36] Naik N, Shembekar P. Elastic behavior of woven fabric composites: III—Laminate design. J Compos Mater 1992;26:2522–41.
[37] Shembekar P, Naik N. Elastic behavior of woven fabric composites: II—Laminate analysis. J Compos Mater 1992;26:2226–46.
[38] Jun Z. Effects of waviness defect on the mechanical properties of fiber reinforced composites: theoretical prediction and experiments investigation. in Chinese with English abstract. Wuhan: Wuhan University of Technology; 2016.
[39] Sheng SZ, Van Hoa S. Three dimensional micro-mechanical modeling of woven fabric composites. J Compos Mater 2001;35:1701–29.
[40] Daniel IM, Ishai O. Engineering mechanics of composite materials. New York: Oxford University Press; 1994.
[41] Naik NK. Woven fabric composites. Lancaster: Technomic Publishing Co., Inc; 1994.
[42] Staab G. Laminar composites. Butterworth-Heinemann 2015.
[43] Bert CW. Classical Lamination Theory. In: Pendleton RL, Tuttle ME, editors. Manual on Experimental Methods for Mechanical Testing of Composites. Dordrecht: Springer, Netherlands; 1989. p. 11–6.
[44] Kollegal MG. Sridharan SJJoCM. A simplified model for plain woven fabrics 2000; 34:1756–86.
[45] Ishikawa T. Chou T-WJJocm. Elastic behavior of woven hybrid composites 1982; 16:2–19.
[46] Ishikawa T, Chou T-W. One-dimensional micromechanical analysis of woven fabric composites. AIAA journal 1983;21:1714–21.
[47] Xiong J, Shenoi R, Cheng X. A modified micromechanical curved beam analytical model to predict the tension modulus of 2D plain weave fabric composites. Compos B Eng 2009;40:776–83.